Absolute nonradiative energy-conversion-efficiency spectra in $Ti^{3+}:Al_2O_3$ crystals measured by noncontact quadrature photopyroelectric spectroscopy

A. Mandelis, J. Vanniasinkam, and S. Budhudu
Photothermal and Optoelectronic Diagnostics Laboratory, Department of Mechanical Engineering, University of Toronto, Toronto, Canada M5S 1A4

A. Othonos
Ontario Laser and Lightwave Research Center, University of Toronto, Toronto, Canada M5S 1A4

M. Kokta
Union Carbide, Incorporated, Washougal, Washington 98671
(Received 8 March 1993)

Photopyroelectric spectroscopy (PPES) was used in a noncontact experimental configuration to obtain high-resolution absolute spectra of the optical-to-thermal energy-conversion efficiency (nonradiative coefficient), $\eta_{NR}(\lambda)$, of Ti:sapphire laser crystals with widely different figures of merit. Optical-absorption-coefficient $\beta(\lambda)$ spectra were obtained from the PPES signal in the purely optical transmission mode. These were subsequently used self-consistently in a theoretical model along with PPES-signal quadrature spectra (purely thermal transmission mode) to extract $\eta_{NR}(\lambda)$ spectra. These spectra were found to depend on the optical quality of the bulk and of the polished surfaces of the Ti:sapphire material. Therefore, they can be used for fundamental energy-conversion studies of the excited-state deexcitation manifold, as well as for establishing a practical monitoring criterion of crystal growth and processing quality in $Ti^{3+}:Al_2O_3$.

I. INTRODUCTION AND BACKGROUND

Photoacoustic spectroscopy (PAS) has been utilized to measure values of the luminescence (radiative) quantum efficiencies in optical materials.[1-4] The advantage of this technique, and related photothermal methods, over purely optical methods is the ability to measure the *absolute* nonradiative quantum efficiency, $\eta_{NR}^{(Q)}$.[5-8] This, in turn, can be readily used to determine the *absolute* radiative quantum efficiency, $\eta_R = 1 - \eta_{NR}^{(Q)}$, without recourse to complicated and often inaccurate absolute detector calibration procedures such as the integrating sphere method, or knowledge of absolute ion concentrations in the case of solid-state laser media.[4] In a number of instances, it is the nonradiative quantum efficiency itself which is the important quantity to be determined, such as in the study of nonradiative relaxation of ions in crystals[3] and in powdered samples.[6] Typically, combinations of PAS and another optical technique are required for this type of measurement: Comparisons of PA spectra and optical absorption spectra allow, in principle, the monitoring of thermal energy release channels in deexciting solids, as well as the estimation of relaxation mechanism probabilities, when combined with theories for the shape of absorption bands, such as the Huang-Rhys model[9] or more involved models in the case of complex ions, such as the $Ti^{3+}:Al_2O_3$ system.[10,11]

The measurement of nonradiative energy conversion efficiencies is also important as a criterion of the optical quality of laser materials. For this reason, dependable and accurate values of the optical-to-thermal (nonradiative) energy conversion coefficient are essential. It is, therefore, very desirable to use a single photothermal technique, rather than combinations with optical spectroscopies, to perform this measurement self-consistently. PAS detection can yield such a measurement dynamically via the phase channel as a function of light intensity modulation frequency.[12] Quimby and Yen[13] have used this technique with solid-state laser materials to simultaneously estimate *both* the nonradiative quantum efficiency and the metastable lifetime in ruby. Shand performed similar measurements with alexandrite,[14] and Lima *et al.* used the PA phase technique to measure the nonradiative relaxation time constants of Co^{2+} and Cu^{2+} dopants in soda-lime glasses.[15] Unfortunately, the PA phase detection technique is intrinsically severely limited to low-frequency measurements (<5 kHz) by the significant rolloff of the microphone transfer function[12] and by the inverse proportionality between the PA signal and the modulation frequency, f.[16] This important drawback limits the acceptable signal-to-noise ratio (SNR) to a range of optical materials with lifetimes, τ, of several hundred μs, at best. A variant of this technique based on the extrema in the phase and the amplitude

0163-1829/93/48(10)/6808(14)/$06.00

slope of the modulated infrared photothermal radiometric (PTR) signal was recently introduced in our laboratory[17] and has been applied successfully to ruby laser rods. Commonly with other photothermal techniques, the PTR f^{-1} signal magnitude dependence yielded a SNR too low to derive meaningful values of the parameters $\eta_{NR}^{(Q)}$ and τ when applied to the Ti^{3+}:Al_2O_3 system.[18] For this material the expected extrema in the PTR amplitude and phase occur in the neighborhood of $f \sim 100$ kHz, due to the short metastable level ^2E lifetime $\tau \simeq 3.3\,\mu$s at room temperature.[19]

From the above it can be concluded that dynamic frequency-domain photothermal-based methods, although attractive because they can be used single-ended and self-consistently for nonradiative quantum efficiency measurements, cannot be used with fast relaxing solid-state laser materials due to their limited dynamic range. On the other hand, combined photothermal and optical spectroscopic methods can be used without such limitations, yet they invariably lead to compromised measurement accuracy due to the increased number of experimental operations required by such independent methodologies, which must also include different calibration procedures. These procedures would be difficult, or impossible, to apply with high-quality optical materials, which only generate minute thermal-wave signals.

II. PHOTOPYROELECTRIC SPECTROMETER DESIGN

To overcome these serious difficulties we have successfully considered a particular modification of photopyroelectric spectroscopy (PPES) as a unique, single-ended method, which combines *purely* optical and *purely* thermal modes, *both* in one experimental setup.[20] In conventional PPES, when the nonradiative energy conversion coefficient, η_{NR}, of an optical or optoelectronic material is relatively high ($\gtrsim 10\%$), simple amplitude and phase measurements with the sample thermally isolated from the detector (purely optical mode), or in thermal-wave contact with the detector (mixed optical *and* thermal mode) can be combined to yield high-quality $\eta_{NR}(\lambda)$ spectra. This has been the case with amorphous semiconducting thin films[21,22] and with bulk semiconductor substrates.[23] In the case of transparent, high-quality optical materials, however, $\eta_{NR}(\lambda)$ is typically expected to be a maximum of a few percent.[13,14] For this type of measurement conventional PPES is hard to use because the small thermal contribution to the signal must be extracted very accurately from the mixed optical and thermal modes. This represents a situation where the direct optically transmitted energy through a sample generates optical heating *in the detector,* which is usually at least 1 order of magnitude higher than the purely thermal-wave component which results from optical absorption followed by optical-to-thermal energy conversion and the subsequent heat release *in the solid sample.* Coufal[24] and Dupin, Angru, and Zhaoyong[25] have succeeded in separating out the mixed PPES component from Nd_2O_3 thin films and thin powdered layers, respectively, into its two constituents by phase discrimination between these two channels: The optical transmission-induced signal in the pyroelectric transducer (a polyvinylidene fluoride, PVDF, thin film) appears in phase with the modulation source (after proper phase calibration), whereas the sample-related, purely thermal-wave signal appears out of phase due to its much slower propagation velocity through the body of the sample or through the transparent substrate (so-called "phase shifter"[24]) on which the sample rests. Christofides *et al.*[26] first applied the phase-shifter method to the measurement of thin-film subgap optical absorption coefficient spectra in amorphous silicon thin films deposited on crystalline silicon. These authors obtained an instrumental sensitivity limit of $\beta l \approx 5 \times 10^{-3}$ for 500 Å *a*-Si on *c*-Si, with the latter substrate playing the role of the transparent phase shifter in the subgap spectral range (1200–1500 nm).

In order to measure dependably and accurately the nonradiative energy-conversion-coefficient spectra of Ti^{3+}:Al_2O_3 crystals in this work, we concluded that the phase-shifter concept, although correct in principle, cannot yield the stringent reliability and accuracy required if $\eta_{NR}(\lambda)$ measurements are to be useful in theoretical spectroscopic models,[10,11] as well as in industrial practice, for crystal growth and processing control. This is so because (i) directly transmitted light through the transparent crystal impinges on the PPE detector and causes small but significant dc drifts of its pyroelectric response due to dc temperature changes. These drifts induce phase changes on the order of 0.5°–1°, which can dominate any phase shifts due to the actual crystal heating; (ii) phase shifters of constant thickness, such as transparent substrates[24,26] or optically thin sample layers[25] are neither truly transparent when compared to laser materials of high optical quality, nor flexible enough in their thickness value to assure the necessary combination of purely optical and truly thermally thick mode operations, with the modulation frequency as the adjustable parameter which controls, *and only in principle,* the type of working mode of a given PPES experiment.[23]

Therefore, in this work we further developed our original PPE spectrometer[21,26] to incorporate a variable thickness air layer between sample backsurface and PVDF pyroelectric detector, to play the role of thickness-adjustable, truly transparent phase shifter, which is also used as PVDF dc drift compensator *and* as thermal contact resistance eliminator. Furthermore, the lock-in quadrature signal was monitored, rather than the phase channel,[24] in our experiments, for two reasons: (a) The complete one-dimensional theoretical analysis of the signal also developed in this work yields a simpler expression for the quadrature (i.e., the imaginary part of the complex ac temperature) directly proportional to the desired quantity $\eta_{NR}(\lambda)$. (b) Experimentally, it was found that the quadrature is more stable than the PPE phase, and thus more sensitive to minute signal changes by a factor of $\gtrsim 3$. This has been attributed to the fact that the lock-in phase does involve the in phase (IP) as well as the quadrature (Q) components. Therefore, phase stability is subject to any small direct optical signal fluctuations. These may dominate the quality of the phase channel output, since the latter is up to 2 orders of magnitude lower than the in-phase signal for transparent ma-

terials. In quadrature PPE detection, which acts as a very efficient optical background signal filter, the noise sources are entirely thermal and indirect (i.e., following heat release in the optically excited sample). On the other hand, in-phase PPE detection is mostly dominated by direct, photothermal noise of light impinging on the detector and locally converted into heat. As a result, the phase signal cannot fully compensate for fluctuations in the directly transmitted signal, but involves both optical heating and purely thermal noise sources, while the quadrature signal involves thermal noise only.

The described PPES system design and the concomitant theory have allowed high-resolution, absolute VIS-range measurements of the nonradiative energy-conversion-efficiency spectra from optical quality $Ti^{3+}:Al_2O_3$ samples for the first time. The spectra were obtained self-consistently from two PPE measurements under identical conditions and at a low modulation frequency ($f \ll \tau^{-1}$), using two detector-sample surface distances (i.e., air layer thicknesses).

III. THEORY OF NONCONTACT PPES

In order to analyze quantitatively PPE quadrature data from transparent materials which are very weak sources of thermal waves, the approximate theoretical formulations presented by Coufal[24] and by Christofides *et al.*[26] are inadequate and must be replaced by a general one-dimensional treatment which takes into account all energy pathways and determines explicitly the dependence of the PPES signal on each and all system parameters. Figure 1 shows the one-dimensional theoretical geometry: An optical beam of intermittently modulated intensity and wavelength λ impinges on a transparent solid of thickness l, optical-to-thermal (nonradiative) energy conversion efficiency $\eta_{NR}(\lambda)$, optical absorption coefficient $\beta(\lambda)$, and optical reflectance $R_s(\lambda)$. The backing material is an air gap of (variable) thickness L, interposed between the sample and the PVDF pyroelectric detector. The thickness of the pyroelectric detector element is assumed to be large (semi-infinite) compared to the thermal diffusion length at the working modulation frequency.[20] A thermal source is formed in the solid following absorption and nonradiative deexcitation according to the following mechanisms: (a) Fractional transmission of the optical beam through the bulk of the solid, including multiple reflections at the solid-air interfaces. Figure 2 shows several interreflections and their contributions to depth x in the solid. Odd and even powers of R_s can be summed up in a geometric series yielding the result

$$I(x)=\sum_{n=1}^{\infty} I_n(x)$$
$$=I_0\left[\frac{1-R_s}{1-R_s^2e^{-2\beta l}}\right][e^{-\beta x}+R_s e^{-\beta(2l-x)}]\,. \quad (1)$$

(b) Reflection of the light transmitted through the sample by the metal electrode (coating) of the detector. The reflected energy is sizable, on the order of 45–65 % in the VIS range, Fig. 3. As a result, it can be shown that the contribution of this reflected optical source, incident on the sample at $x=l$, is given by

$$J(x)=R_pI(l)\left[\frac{(1-R_s)e^{-\beta l}}{1-R_s^2e^{-2\beta l}}\right]$$
$$\times[e^{-\beta(l-x)}+R_s e^{-\beta(l+x)}]\,, \quad (2a)$$

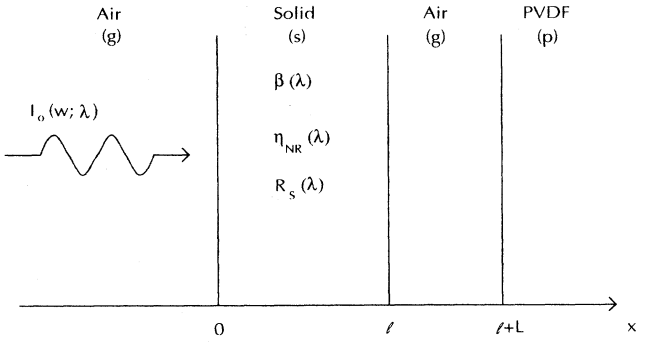

FIG. 1. Experimental geometry for the theoretical analysis of noncontact PPES of a transparent sample of thickness l, optical absorption coefficient $\beta(\lambda)$, and nonradiative energy-conversion efficiency $\eta_{NR}(\lambda)$. Air layer thickness L; semi-infinite PVDF detector. Optical modulation angular frequency: ω; incident optical intensity I_0.

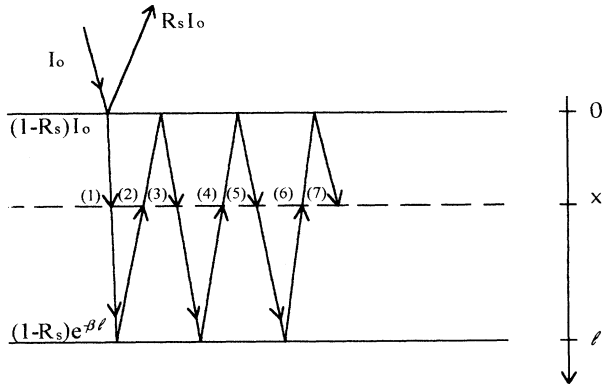

(1): $I_o\,(1-R_s)\,e^{-\beta x}$
(2): $I_o\,(1-R_s)\,R_s\,e^{-\beta(2\ell-x)}$
(3): $I_o\,(1-R_s)\,R_s^2\,e^{-\beta(2\ell+x)}$
(4): $I_o\,(1-R_s)\,R_s^3\,e^{-\beta(4\ell-x)}$
(5): $I_o\,(1-R_s)\,R_s^4\,e^{-\beta(4\ell+x)}$
(6): $I_o\,(1-R_s)\,R_s^5\,e^{-\beta(6\ell-x)}$
(7): $I_o\,(1-R_s)\,R_s^6\,e^{-\beta(6\ell+x)}$
⋮

FIG. 2. Cross-sectional schematic of a solid of reflectance $R_s(\lambda)$, optical absorption coefficient $\beta(\lambda)$, and thickness l, showing contributions of the first seven interreflections to the optical intensity at depth x.

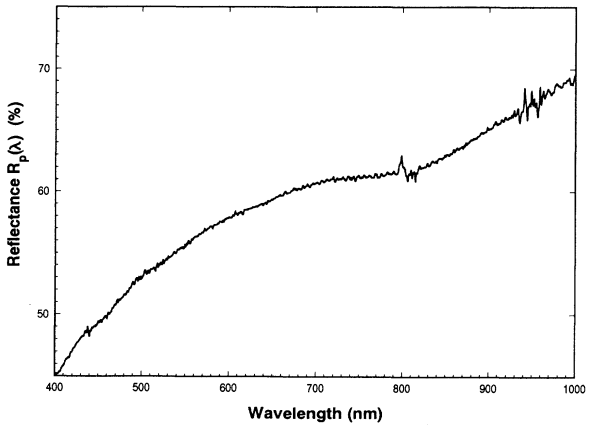

FIG. 3. Reflectance spectrum, $R_p(\lambda)$, of Kynar® PVDF metallized with Al/Ni coating.

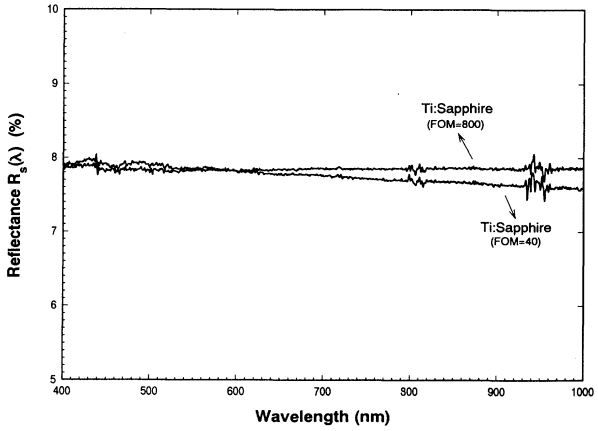

FIG. 4. Reflectance spectra, $R_s(\lambda)$, of 2.0-cm-thick Ti:sapphire crystals with FOM=40 and 800.

where Eq. (1) gives

$$I(l)=I_0\left[\frac{1-R_s^2}{1-R_s^2e^{-2\beta l}}\right]e^{-\beta l}\ . \tag{2b}$$

In Eqs. (2), $R_p(\lambda)$ is the reflectance of the metallized PVDF detector and can be determined experimentally. Notice that higher fractional orders of reflected light from the detector need not be considered due to the low value range of $R_s(\lambda)$, also determined experimentally ($<10\%$ in the spectral range 400–1000 nm, Fig. 4). The sum of Eqs. (1) and (2) gives the total optical energy contribution to depth x in the solid:

$$I_t(x)=I(x)+J(x)=I_0\left[\frac{1-R_s}{1-R_s^2e^{-2\beta l}}\right]F(x)\ , \tag{3a}$$

where

$$F(x)\equiv N_1e^{-\beta x}+N_2e^{-\beta(2l-x)}\ , \tag{3b}$$

$$N_1\equiv 1+R_sR_p(1+R_s)e^{-2\beta l}\ , \tag{3c}$$

$$N_2\equiv R_s[1+R_p(1+R_s)]\ . \tag{3d}$$

Now we may turn to the coupled thermal-wave equations in the air-solid-air-pyroelectric geometry of Fig. 1:[20]

$$\frac{d^2T_g}{dx^2}-\sigma_g^2T_g=0,\quad x\le 0 \text{ and } l\le x\le l+L\ , \tag{4a}$$

$$\frac{d^2T_p}{dx^2}-\sigma_p^2T_p=0,\quad x\ge l+L\ , \tag{4b}$$

$$\frac{d^2T_s}{dx^2}-\sigma_s^2T_s=-\eta_{\rm NR}(\lambda)\beta(\lambda)\left[\frac{I_t(x;\lambda)}{2k_s}\right],\quad 0\le x\le l\ . \tag{4c}$$

In Eqs. (4), $\sigma_j\equiv(1+i)\sqrt{\omega/2\alpha j}$ is the complex thermal diffusion coefficient in material (j) with thermal diffusivity α_j; j:(g,s,p). k_s is the solid thermal conductivity. The wavelength dependence of I_t via the coefficients $\beta(\lambda)$, $R_s(\lambda)$, $R_p(\lambda)$ has been explicitly denoted in Eq. (4c). The solutions to Eqs. (4) giving the ac temperatures in the various regions of Fig. 1 are

$$T_g(x;\omega)=C_1e^{\sigma_g x},\quad x\le 0\ , \tag{5a}$$

$$T_s(x;\omega)=C_2e^{\sigma_s x}+C_3e^{-\sigma_s x}-EF(x)\ , \tag{5b}$$

$$T_g(x;\omega)=C_4e^{-\sigma_g(x-l)}+C_5e^{\sigma_g(x-l)}\ ,\quad l\le x\le l+L\ , \tag{5c}$$

$$E\equiv\frac{I_0\eta_{\rm NR}(\lambda)\beta(\lambda)}{2k_s(\beta^2-\sigma_s^2)}\left[\frac{1-R_s}{1-R_s^2e^{-2\beta l}}\right],\quad 0\le x\le l\ , \tag{5d}$$

and

$$T_p(x;\omega)=C_6e^{-\sigma_p(x-l-L)},\quad x\ge l+L\ . \tag{5e}$$

The standard boundary conditions of temperature and heat flux continuity[20] can be used to determine the coefficients C_j, $j=1-6$. In particular, the heat flux boundary condition at the air-pyroelectric interface $x=l+L$ is written as

$$-k_p\frac{d}{dx}T_p(x;\omega)|_{x=l+L}+k_g\frac{d}{dx}T_g(x;\omega)|_{x=l+L}=I_0(1-R_p)e^{-\beta l}\ , \tag{6}$$

where k_p and k_g are the thermal conductivities of pyroelectric detector and gas (air), respectively. The solution of the system of six algebraic equations in $\{C_1,\ldots,C_6\}$ yields the value of C_6, which is proportional to the PVDF pyroelectric response:

$$C_6=\frac{1}{A}\left\{G\left[\tau-\gamma_{gs}\left[\frac{\xi-\xi^{-1}}{\xi-\gamma_{gs}^2\xi^{-1}}\right]\tau^{-1}\right]-2\left[\frac{b_{gp}}{\xi-\gamma_{gs}^2\xi^{-1}}\right]\left[\xi Q_2-\gamma_{gs}Q_3\xi^{-1}+2\left[\frac{Q_1}{1+b_{gs}}\right]\right]\right\}\ , \tag{7a}$$

where

$$G \equiv \frac{I_0(1-R_p)}{k_p \sigma_p}\left[\frac{1-R_s^2}{1-R_s^2 e^{-2\beta l}}\right] e^{-\beta l}, \tag{7b}$$

$$\tau \equiv e^{\sigma_g L},$$

$$\xi \equiv e^{\sigma_s l},$$

$$\gamma_{ij} \equiv \frac{1-b_{ij}}{1+b_{ij}}, \tag{7c}$$

$$b_{ij} \equiv \frac{k_i\sqrt{\alpha_j}}{k_j\sqrt{\alpha_i}},$$

$$r_s \equiv \beta/\sigma_s,$$

$$Q_1 \equiv -E[r_s(N_1 - N_2 e^{-2\beta l}) + b_{gs}(N_1 + N_2 e^{-2\beta l})], \tag{7d}$$

$$Q_2 \equiv E[N_1 + N_2 + r_s(N_1 - N_2)]e^{-\beta l}, \tag{7e}$$

$$Q_3 \equiv E[N_1 + N_2 - r_s(N_1 - N_2)]e^{-\beta l}, \tag{7f}$$

$$A \equiv \tau(1+b_{gp}) - \tau^{-1}(1-b_{gp})\left[\gamma_{gs}\left[\frac{\xi-\xi^{-1}}{\xi-\gamma_{gs}\xi^{-1}}\right]\right]. \tag{7g}$$

Now the photopyroelectric signal can be written:[27]

$$V(\omega) = \frac{i\omega\tau_E p L_p}{\epsilon(1+i\omega\tau_E)}\langle T_p(x;\omega)\rangle \tag{8}$$

where p is the pyroelectric coefficient, L_p is the thickness of the PVDF detector, τ_E is the RC time constant of the equivalent circuit comprising the pyroelectric element and the preamplifier, ϵ is the dielectric constant of the pyroelectric, and

$$\langle T_p(x;\omega)\rangle = \frac{1}{L_p}\int_{L_p} T_p(x;\omega)dx = \frac{C_6}{\sigma_p L_p}(1-e^{-\sigma_p L_p}). \tag{9}$$

For our semi-infinite, thermally thick PVDF film ($\sigma_p L_p \gg 1$), the PPE voltage response can be written

$$V(\omega) = \frac{i\omega\tau_E p C_6(\omega)}{\epsilon(1+i\omega\tau_E)\sigma_p} \equiv S(\omega)\frac{C_6(\omega)}{\sigma_p}. \tag{10}$$

Here $S(\omega)$ is an instrumental factor which can be experimentally normalized out. Finally, the PPE signal in the geometry of Fig. 1 can be expressed as follows:

$$\begin{aligned} V(\omega) = {} & \frac{I_0 S(\omega)}{k_p \sigma_p^2 (1+b_{gp})}\left[\frac{1-R_s}{1-R_s^2 e^{-2\beta l}}\right] \\ & \times \left\{(1+R_s)(1-R_p)\left[1-\gamma_{gs}\left[\frac{1-e^{-2\sigma_s l}}{1-\gamma_{gs}^2 e^{-2\sigma_s l}}\right]e^{-2\sigma_g L}\right]e^{-\beta l}\right. \\ & + \frac{b_{gs}\eta_{NR}(\lambda)\beta(\lambda)e^{-(\sigma_s l+\sigma_g L)}}{\sigma_s(1+b_{gs})(r_s^2-1)(1-\gamma_{gs}^2 e^{-2\sigma_s l})} \\ & \times \left[\frac{2}{1+b_{gs}}[r_s(N_1 - N_2 e^{-2\beta l}) + b_{gs}(N_1 + N_2 e^{-2\beta l})]\right. \\ & - \{[N_1 + N_2 + r_s(N_1 - N_2)]e^{\sigma_s l} - \gamma_{gs}[N_1 + N_2 - r_s(N_1 - N_2)] \\ & \left.\left.\times e^{-\sigma_s l}\}e^{-\beta l}\right]\right\} \Big/ \left[1-\gamma_{gs}\gamma_{gp}\left[\frac{1-e^{-2\sigma_s l}}{1-\gamma_{gs}^2 e^{-2\sigma_s l}}\right]e^{-2\sigma_g L}\right]. \end{aligned} \tag{11}$$

This equation gives the most general response (MGR) of a PPE noncontact experiment. It is instructive to consider several special cases of experimental importance to this work.

(1) Optically opaque solids, $\beta l \gg 1$:

$$e^{-\beta l} \simeq 0, \quad |r_s| \gg 1, \quad N_1 = 1.$$

Then Eq. (11) reduces to

$$V(\omega) = 2S(\omega)I_0(1-R_s)\frac{b_{gs}\eta_{NR}}{k_p\sigma_p^2(1+b_{gp})(1+b_{gs})^2} \times \left[\frac{e^{-\sigma_s l}}{1-\gamma_{gs}^2 e^{-2\sigma_s l}}\right]\left[\frac{e^{-\sigma_g L}}{1-\gamma_{gs}\gamma_{gp}e^{-2\sigma_g L}}\right]. \tag{12}$$

Equation (12) shows that (i) all optical absorption

coefficient information concerning the solid vanishes, as expected under PPE saturation;[20] (ii) the signal is purely thermal in nature and exhibits the familiar strong decays in magnitude through sequential passage across the body of the solid and the gas; (iii) there is a possibility of optical information about the solid surface through the signal dependence on the surface reflectance $R_s(\lambda)$.

(2) Absence of a solid layer: $l=0$. In this limit it can be shown with a straightforward but tedious manipulation that the MGR reduces to

$$V_R(\omega)=\frac{S(\omega)I_0[1-R_p(\lambda)]}{k_p\sigma_p^2(1+b_{gp})} . \tag{13}$$

This expression is as expected from direct incidence of an optical beam on the pyroelectric surface[20] and Eq. (13) serves as a normalizing reference signal.

(3) Purely optical transmission mode: $L\rightarrow\infty$. In this case the MGR gives

$$V_\infty(\omega)=\frac{S(\omega)I_0(1-R_p)}{k_p\sigma_p^2(1+b_{gp})}\left[\frac{1-R_s^2}{1-R_s^2e^{-2\beta l}}\right]e^{-\beta l} . \tag{14}$$

No thermal information about the solid can be obtained, since the sample and the detector are entirely decoupled thermally. This case is important in that a normalized measurement, with and without the solid in place, yields the value of the absolute optical adsorption coefficient, when Eq. (14) is solved for β:

$$\beta(\lambda)=-\frac{1}{l}\ln\left\{\frac{1-R_s^2}{2R_s^2\rho_\infty}\{\sqrt{1+[2\rho_\infty R_s/(1-R_s^2)]^2}-1\}\right\} , \tag{15a}$$

where

$$\rho_\infty(\lambda)\equiv V_\infty(\omega;\lambda)/V_R(\omega;\lambda) . \tag{15b}$$

(4) Mixed thermooptical mode: Application to Ti^{3+}:Al_2O_3 laser materials. The MGR, Eq. (11), can be simplified considerably by considering the value of the thermal coupling coefficient b_{gs} for the case of Ti:sapphire laser crystals. The pertinent solid values are[28]

$$\alpha_s=\frac{k_s}{(\rho c)_s}=\frac{0.33\ \mathrm{W\,cm^{-1}\,K^{-1}}}{3.1\ \mathrm{J\,cm^{-3}\,K^{-1}}}=0.106\ \mathrm{cm^2/s} .$$

The k_g and α_g values for air are $\sim 2.38\times10^{-4}$ $\mathrm{W\,cm^{-1}\,K^{-1}}$ and ~ 0.19 $\mathrm{cm^2/s}$, respectively.[20] These values yield $b_{gs}\simeq 5.4\times10^{-4}$, or $\gamma_{gs}\simeq 0.9989$, Eq. (7c). Similarly,[20] $b_{gp}\simeq 9.76\times10^{-3}$, or $\gamma_{gp}\simeq 0.981$. As a result of the near-unity values of γ_{gs},γ_{gp}, a simplification in Eq. (11) can be obtained by setting

$$\frac{1-e^{-2\sigma_s l}}{1-\gamma_{gs}^2e^{-2\sigma_s l}}\simeq\frac{1-\gamma_{gs}e^{-2\sigma_g L}}{1-\gamma_{gs}\gamma_{gp}e^{-2\sigma_g L}}\simeq 1 \tag{16}$$

correct to order $\delta_{gs}(2-\delta_{gs})=2.2\times10^{-3}$, where $\delta_{gs}\equiv 1-\gamma_{gs}$; and to order $\delta_{gp}=1.9\times10^{-2}$, where $\delta_{gp}\equiv 1-\gamma_{gp}$, respectively. Under approximations (16), the MGR equation (11) normalized by the direct detector response $V_R(\omega;\lambda)$, Eq. (13), reduces to

$$\begin{aligned}\frac{V_L(\omega;\lambda)}{V_R(\omega;\lambda)}=&\left[\frac{1}{1-R_s^2e^{-2\beta l}}\right]\left[(1-R_s^2)e^{-\beta l}+\frac{\eta_{\mathrm{NR}}(\lambda)}{1-R_p}\left[\frac{b_{gs}}{1+b_{gs}}\right]\left[\frac{r_s}{r_s^2-1}\right]\left[\frac{1}{1-\gamma_{gs}^2e^{-2\sigma_s l}}\right]\left[\frac{e^{-\sigma_g L}}{1-\gamma_{gs}\gamma_{gp}e^{-2\sigma_g L}}\right]\right.\\
&\times\left[\frac{2}{1+b_{gs}}[r_s(N_1-N_2e^{-2\beta l})+b_{gs}(N_1+N_2e^{-2\beta l})]e^{-\sigma_s l}\right.\\
&-[N_1+N_2+r_s(N_1-N_2)\\
&\left.\left.-\gamma_{gs}\{N_1+N_2-r_s(N_1-N_2)\}e^{-2\sigma_s l}]e^{-\beta l}\right]\right| .\end{aligned} \tag{17}$$

The structure of Eq. (17) is reminiscent of earlier, less complete, equations reported in Refs. 24 and 26: The first term in the large square bracket on the right-hand side is the result of direct optical transmission after infinite interreflections through the solid, including a source due to the strong reflection from the metallized surface of the PVDF detector. This term then corresponds to the purely optical mode. The second term is the result of the optical heating of the solid due to absorption and subsequent thermalization. It is proportional to the thermal coupling coefficient, b_{gs}, as expected from the thermal energy release across the solid-gas back interface ($b_{gs}\ll 1$); it is further proportional to the desired quantity, $\eta_{\mathrm{NR}}(\lambda)$, also a small number in optical materials. The rest of the solid constituents of this term involve the optical and geometrical properties of the solid, a fact that renders the term into a mixed thermooptical mode. Finally, there is an important L dependence in this second term, which plays the role of the thermal-wave phase shifter[24,26] with controlled thickness and zero absorption. It is important to note that the first term on the rhs of Eq. (17) is real, whereas the second term is complex, small in magnitude, and directly proportional to $\eta_{\mathrm{NR}}(\lambda)$. Based on the structure of Eq. (17), a polar coordinate representation may be written in the following form:

$$\frac{V_L(\omega;\lambda)}{V_R(\omega;\lambda)}=\left[\frac{1}{1-R_s^2e^{-2\beta l}}\right]\left\{(1-R_s^2)e^{-\beta l}+\eta_{\mathrm{NR}}(\lambda)\left[\frac{b_{gs}}{1+b_{gs}}\right]\frac{|r_s|e^{-a_gL}}{(1-R_p)|Z_1||Z_2||Z_3|}\right.$$
$$\left.\times\left[2\left[\frac{|Z_4|}{1+b_{gs}}\right]e^{-a_sl}e^{-i\psi_1}-(|Z_5|e^{-i\psi_2}-\gamma_{gs}|Z_6|e^{-2a_sl}e^{-i\psi_3})e^{-\beta l}\right]\right\}, \tag{18a}$$

where

$$|r_s|=\frac{\beta}{\sqrt{2}a_s},\quad a_j=\sqrt{\omega/2\alpha_j},\quad j=g,s\ . \tag{18b}$$

The rest of the terms appearing in Eq. (18a) are given in the Appendix. Based on Eq. (18), two consecutive measurements can clearly give self-consistent values of $[\beta(\lambda),\eta_{\mathrm{NR}}(\lambda)]$: (a) With the detector position at "infinity" (i.e., $L\gg a_g^{-1}$), we obtain

$$\frac{V_{L\to\infty}(\omega;\lambda)}{V_R(\omega;\lambda)}=\rho_\infty(\lambda)=\frac{(1-R_s^2)e^{-\beta l}}{1-R_s^2e^{-2\beta l}}\ . \tag{19}$$

This equation gives the absorption coefficient directly if $R_s(\lambda)$ is known. Thus, we retrieve the purely optical mode, Eq. (15). (b) With the detector-solid sample distance at "infinity" the lock-in analyzer phase is set to zero, either in the absence or in the presence of the transparent sample. Then the sample-detector position decreases sufficiently, so that a nonzero lock-in *quadrature* S_Q signal appears. This is the thermooptical mode. When normalized by the detector response, theoretically, this operation corresponds to taking $\mathrm{Im}[V_L(\omega;\lambda)/V_R(\omega;\lambda)]$ in Eq. (18):

$$S_Q(\lambda;L)\equiv\mathrm{Im}[V_L(\omega;\lambda)/V_R(\omega;\lambda)]$$
$$\simeq-\eta_{\mathrm{NR}}(\lambda)b_{gs}\left[\frac{1}{[1-R_p(\lambda)][1-R_s^2(\lambda)e^{-2\beta l}]}\right]\left[\frac{|r_s(\lambda)|}{|Z_1(\lambda)||Z_2(L)||Z_3(L)|}\right]$$
$$\times\{2|Z_4(\lambda)|e^{-a_sl}\sin\psi_1(\lambda;L)-[|Z_5(\lambda)|\sin\psi_2(\lambda;L)-\gamma_{gs}|Z_6(\lambda)|e^{-2a_sl}\sin\psi_3(\lambda;L)]e^{-\beta l}\}\ . \tag{20}$$

The most important dependences in Eq. (20) are those on λ and L, since the geometry of Fig. 1 allows the PPES measurements for $(\beta,\eta_{\mathrm{NR}})$ determination to be performed at a single modulation frequency, by varying the distance L. This configuration optimizes the accuracy of the technique because there is no need to account for the (usually unknown) transfer function of the instrumentation. Furthermore, it is clear from Eqs. (18) and (20) that the selection of the quadrature signal, $S_Q(\lambda;L)$, efficiently suppresses the very large direct optical contribution to the PPE signal, which appears in the IP channel of the lock in. Using the $\beta(\lambda)$ values obtained in step (a) in Eq. (20), along with the easily predetermined values of $R_p(\lambda)$ and $R_s(\lambda)$, the quadrature channel yields the purely thermal mode, i.e., $\eta_{\mathrm{NR}}(\lambda)$. Absolute (quantitative) spectra can thus be obtained with careful measurements of the $S_Q(\lambda;L)$ dependence on L. This quantity must be known very accurately; in this work it was estimated by fitting the PPE data to the theoretical signal-dependence curve on L.

IV. EXPERIMENT AND RESULTS: $\beta(\lambda)$ AND $\eta_{\mathrm{NR}}(\lambda)$ PPE SPECTRA

A. Materials preparation

Crystals of Ti:Al_2O_3 were grown by the Czochralski pulling technique from a molten mixture of Al_2O_3-Ti_2O_3. The starting materials used were 99.999% pure (Al_2O_3; Ti_2O_3). The growth conditions were pulling rate=0.3 mm/h, rotation rate=5 rpm, ambient atmosphere was purified argon, the seed was sapphire 90° (off C axis) A orientation. The starting materials were melted by means of RF heating in an iridium crucible. Crystals were grown 2.5″ in diameter and 10″ long. A postgrowth treatment process was applied, based on earlier practice at Union Carbide. The grown crystals were annealed at 1850 °C for 20 h in an atmosphere of 50% H_2 and 50% Ar. Some samples were cut from the boule following this treatment. These samples exhibited low figure of merit (FOM≈40). Several samples were then prepared from crystals subjected to further annealing in pure H_2 at 1940 °C for 180 h. This type of treatment is known to improve the quality of Czochralski-grown Ti^{3+}:Al_2O_3.[29] As a result, the overall optical quality of the crystal improved, yielding a much higher figure of merit (FOM≈800). Finally, all samples were subjected to "low-temperature" annealing at 1100 °C for 12 h, following the "rough" fabrication (slicing and grinding). Thin and thick batches of samples were thus prepared and polished, and the FOM were measured.

B. Instrumentation and spectroscopy

The reflectance spectra of the PVDF detector with Al-Ni coating[30] and of the Ti:sapphire samples are shown in

Figs. 3 and 4, respectively. The experimental value thus obtained was used in subsequent calculations, whenever $R_p(\lambda)$ and $R_s(\lambda)$ values were required. Noncontact photopyroelectric spectra were then obtained using instrumentation conforming to the geometry of Fig. 1. The schematic of this apparatus, a modification of our earlier PPE spectrometer,[26] is shown in Fig. 5. The 1000-W Xe-lamp spectral throughout was f-number matched to the entrance of the monochrometer (MC). The output radiation was collimated with the lenses (L) and chopped with a mechanical chopper (C), before impinging on the polished surface of the crystal (S). The sample (S)-PPE detector (D) assembly was mounted on optical benches supplied with micrometer stages, which allowed the distance between them to vary from ~ 100 μm to "infinity" (~ 5 mm), by either moving the sample or the detector. Positional dependence of the PPE signal was minimized by placing the detector surface at the beam waist of the focused radiation. This proved to be a necessary correction procedure for some samples and/or wavelengths in which the PPE quadrature signal was so low as to be on the same order as the positional dependence due to intensity variations of the incident beam, resulting from its slow spatial convergence (or divergence). The alternate procedure of varying the sample position proved to be generally satisfactory and gave spectra of similar quality to the detector position variation.

Two sets of Ti^{3+}:Al_2O_3 crystals were studied: One set consisted of long (thick) rods, ~ 1 cm in diameter and 2 cm in length comprising high and low FOM samples. The other set consisted of thin (<0.13 cm) disks of the same diameter and from the same materials. Optical absorption coefficients were obtained photopyroelectrically in the purely optical transmission mode using Eq. (15). The condition $L \rightarrow \infty$ could be satisfied in the thermally thick gas layer for $L \gtrsim 5$ mm, at chopping frequency $f = 9$ Hz. At $L \simeq 1$ cm the PPE signal quadrature was zeroed and the sample holder was slid sideways and out of the beam path on the optical bench to record the lamp spectrum, $V_R(\omega;\lambda)$ (see double arrow above S in Fig. 5). With the sample back in place, the spectrum of the light transmitted through the transparent crystal was recorded, corresponding to $V_\infty(\omega;\lambda)$ in Eq. (15b). We found it important to record these two spectra within the same experimental period for each sample and after complete thermalization of the instrumentation (~ 1 h after turn on), in order to obtain adequate quantitative reproducibility of the $\eta_{NR}(\lambda)$ spectra. The absolute values of $\beta(\lambda)$ are shown in Fig. 6 for four Ti^{3+}:Al_2O_3 samples. These spectral features and values were subsequently verified by conventional transmittance spectroscopy.

Thermal energy generation spectra were recorded at each wavelength after the "infinite distance" (purely optical) measurement was made, by decreasing the distance L to some predetermined value <1 mm at which a measurable stable quadrature signal was present. Although, in principle, nulling the Q channel at $L \rightarrow \infty$ at one wavelength is sufficient for the entire spectrum, in practice, the strong optical transmission variations of the Ti^{3+} ion across the spectrum induced small changes in the PVDF detector phase, a result of different dc optical heating levels of the polymer. These changes were $\sim 0.5°$ and were found to interfere with our measurements of phase variations due to thermal-wave generation in the crystals. Therefore, in these experiments the quadratures of the signals corresponding to "infinite" and "finite" L distances were subtracted at each wavelength. A further correction was made whenever the positional variation of the Q signal was significant ($>10\%$) on the scale of the magnitude of the spatial profile of the generated thermal wave in the gas column. This only occurred with the weakest signals from the thick FOM = 800 sample.

If qualitative $\eta_{NR}(\lambda)$ spectra suffice, absolute knowledge of the particular L value at which the spectra are recorded is not necessary, as long as the $\beta(\lambda)$ spec-

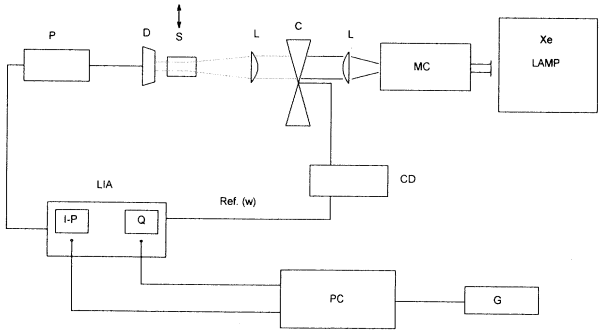

FIG. 5. Schematic of noncontact PPES spectrometer. MC, monochromator; L, lens; C, chopper; S, sample; D, detector; P, preamplifier with adjustable band-pass filters; LIA, lock-in-amplifier (EG&G Model 5209 in the IP and Q modes); CD, chopperdriver; PC, computer for data acquisition, processing, and theoretical analysis; G, graphics and plotter.

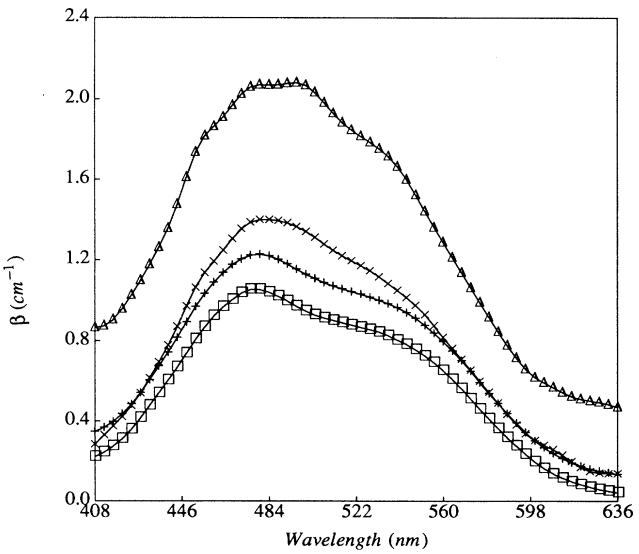

FIG. 6. Optical absorption spectra of Ti^{3+}:Al_2O_3 crystals, obtained with PPES in the purely optical transmission mode, Eq. (15), at $f = 9$ Hz. (△-△-△): $l = 0.0813$ cm, FOM = 40; (×-×-×): $l = 0.1295$ cm, FOM = 800; (+-+-+): $l = 2.0169$ cm, FOM = 40; and (□-□-□): $l = 2.0125$ cm, FOM = 800.

trum is known and the other λ-dependent quantities (R_p, R_s) do not exhibit strong spectral gradients. This transpires from Eq. (20), which shows a simple linear dependence of S_Q on η_{NR}. This feature may be used to produce "rapid-scan" spectra of $\eta_{NR}(\lambda)$ in situations where only relative values matter (e.g., an industrial quality control setting). For the purposes of this work, it was desirable to obtain absolute measurements of $\eta_{NR}(\lambda)$. For this reason, the rapid spatial decay of the thermal wave in the gas, Eq. (17),

$$V_L(\omega;L)=\text{const}\times\left[\frac{e^{-\sigma_g L}}{1-\gamma_{gs}\gamma_{gp}e^{-2\sigma_g L}}\right], \tag{21}$$

necessitates excellent precision in the knowledge of the actual value of L. This can only be achieved upon matching experimental decay profiles to theory, as shown in Fig. 7: The experimental curve always appears at an offset distance with respect to the theoretical profile which gives the absolute distance of the PVDF detector from the surface of the sample. A rigid shift of the experimental curve by 120 μm, as shown, produced the desired absolute best-fit L-value scale by subtracting the offset value from the experimentally measured values. It can be noticed that at distances $L \gtrsim 1.4$ mm from the sample surface an apparent deviation of the Q-signal data from the theoretical thermal-wave profile occurs. This has been tentatively attributed to the violation of the (theoretically assumed) one-dimensionality of the problem at large L values. A stronger optical source will be required to investigate this deviation, due to the very high attenuation of the signal level at these distances, and the concomitant deterioration of the signal-to-noise ratio.

Figure 8 shows respective IP and Q signal levels. The former (direct, purely optical) signal is 2 orders of magnitude stronger than the latter (purely thermal-wave) signal in the case of Ti:sapphire PPES. For Nd_2O_3 thin powders this ratio was ~ 60.[25] For 8×10^{14} Nd_2O_3 molecules in a 1-μm-thick PMMA film coated on top of a 0.1-mm-thick undoped PMMA film on a silver substrate, Coufal measured phase shifts in the 0.1°–0.8° range with his thermal-wave phase shifter.[24] By comparison the phase shifts corresponding to the plots of Fig. 8 are invariably in the 0.02°–0.2° range, due to the high optical (i.e., poor thermal) quality of the Ti:sapphire laser materials in this study.

Nonradiative energy-conversion-efficiency spectra, $\eta_{NR}(\lambda)$, were obtained from thermal energy generation (S_Q signal) spectra, such as the one shown in Fig. 8 (Q), by using the calculated absolute L values in Eq. (20), along with the $\beta(\lambda)$, $R_s(\lambda)$, and $R_p(\lambda)$ spectra determined earlier. These spectra are shown in Fig. 9 for both sets of samples. It can be seen that the η_{NR} values for the thin disk samples are considerably higher (8–26 %) than those for the thick (long-rod) samples (1–7 %). These ranges are consistent with a thermal energy generation measurement performed on Ti:sapphire by Albers *et al.*[19] Those authors used a resistive Wheatstone-bridge circuit to measure heat released by a laser-irradiated sample in intimate contact with a positive-temperature-coefficient (PTC) resistor, by monitoring the change in the electrical characteristics of the PTC resistor in the presence of a heat flux from the sample. They reported radiative quantum efficiencies in the 315–325 K temperature range, consistent with 24–32 % η_{NR} values. In a different experiment using all-optical (integrating sphere) methods,[31] Byvik *et al.*[32] determined the quantum efficiency of

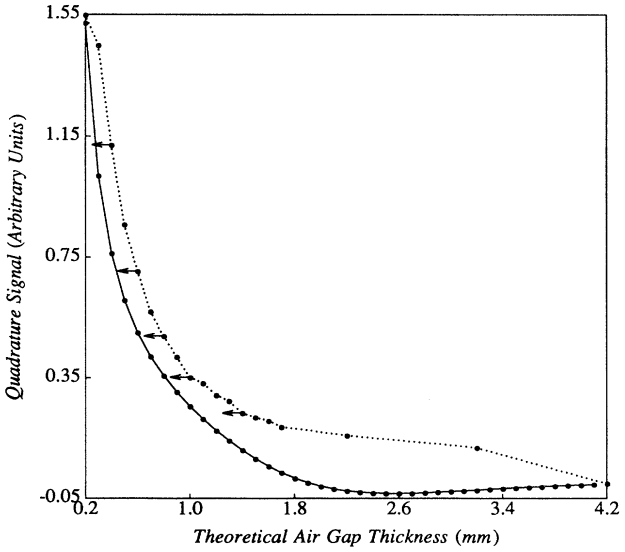

FIG. 7. Spatial decay profiles of the thermal-wave Q signal in the air gap between sample and detector. Solid line: theoretical, $\text{Im}[V_L(\omega;L)]$, Eq. (20). Dotted line: experimental, using the thin Ti:sapphire disk (FOM=40). The arrows indicate a rigid shift by 120 μm. Values in Eq. (20): $\alpha_g=0.19$ cm^2/s, $\gamma_{gs}=0.9989$, $\gamma_{gp}=0.981$; $f=9$ Hz.

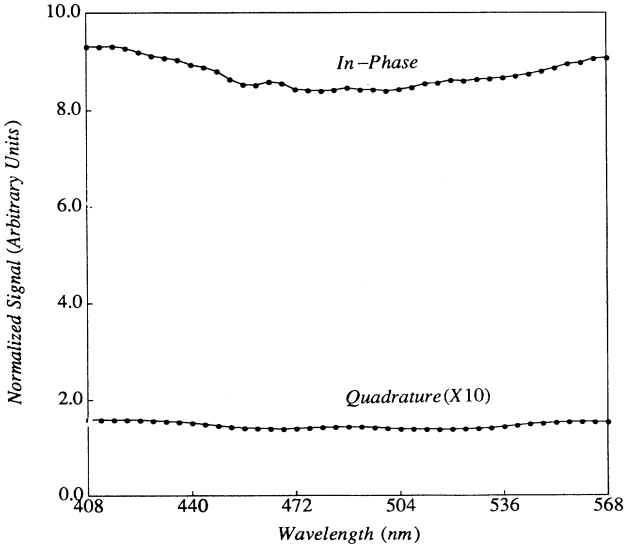

FIG. 8. In-phase (IP) and quadrature (Q) spectrum signal levels from a thin Ti:sapphire disk (FOM=40), normalized by the lamp spectrum at $f=9$ Hz.

Czochralski-grown Ti:sapphire crystals directly from the ratio of luminescent intensity to the adsorbed intensity at the 514.5-nm line from an Ar^+-ion laser. The measured value, $QE = 0.7$, implies a 30% value for η_{NR}. Some of the above-mentioned η_{NR} values are certainly higher than *average* values from our spectra. However, the integrated luminescence measurements, like the one reported in Ref. 32, can only estimate a value for the spectrally integrated thermal energy release, unlike the present spectrally distributed values. This fact accentuates the need for wavelength-resolved η_{NR} measurements. In recent publications Li *et al.*[33,34] have presented a dc thermal technique for measuring η_{NR} in laser materials, by comparing relative optical powers required to raise the absorbing crystal and a black surface patch to the same dc temperature. The η_{NR} values thus obtained were in the 40–55 % range for $Cr^{3+}:Al_2O_3$, and in the 60% range for $Ti^{3+}:Al_2O_3$. Furthermore, a slight monotonic decrease of η_{NR} with increasing wavelength was observed in the 450–510 nm range in $Ti^{3+}:Al_2O_3$. This trend is consistent with our spectra, Fig. 9. The absolute η_{NR} values calculated in Ref. 34 are seemingly too high when compared with ours, and no spectral details in the $\lambda > 510$ nm range have been reported. An explanation of these discrepancies may be given in terms of surface absorptions leading to phenomenologically higher η_{NR} values with the dc thermal technique. No such effects were considered by those authors, yet their evocation is crucial to understanding the trends shown in Fig. 9, as will be discussed below.

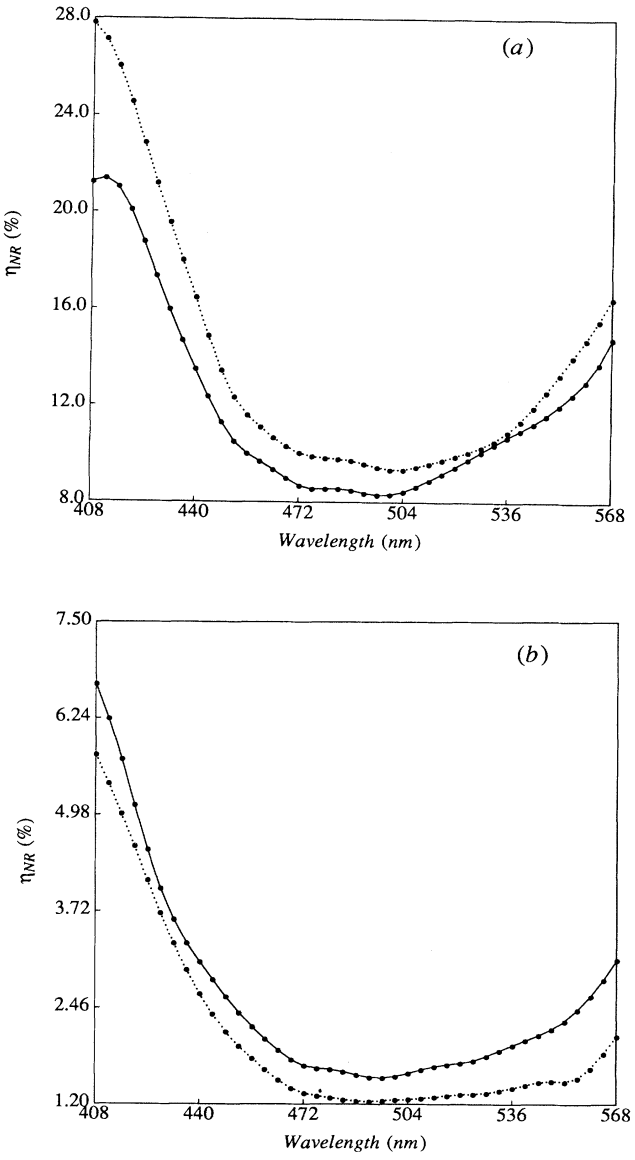

FIG. 9. Nonradiative energy-conversion-efficiency spectra of the Ti:sapphire crystals. (a) Thin samples: solid line, FOM=800; dotted line, FOM=40. (b) Thick samples: solid line, FOM=800; dotted line, FOM=40.

V. DISCUSSION

The spectral line shapes of the optical absorption coefficients, Fig. 6, are typical of the $Ti^{3+}:Al_2O_3$ system. These consist of a broad peak centered around 470 nm, which corresponds to the $^2T_{2g} \rightarrow {}^2E_g$ transition broadened by phonons. The shoulder on the low-energy side is due to Jahn-Teller splitting of the ^2E_g (upper) state.[35] The thick samples exhibit smooth absorption curves, with the absorption coefficient of the FOM=800 sample somewhat lower. This is in agreement with previous observations,[29] which have established that annealed Ti:sapphire samples exhibit lower absorption profiles, due to the reduction in certain kinds of point defects and the relaxation of Ti^{3+} from interstitial or defect sites in the desired Al^{3+} sites.

Considerably higher absorption coefficients, however, were measured with the thin disk samples, Fig. 6. As in the case of the thick samples, the trends for lower absorption with increased degree of annealing can also be seen in the thin sample absorption. The secondary peaks in the 440–490 nm range of these spectra do not usually appear in other published literature spectra.[29,32,35] The strong optical absorptions in the thin disks are accompanied by high values of η_{NR} in the optically active region, at, or above, the upper ^2E level absorption range (480–500 nm). Similarly, below the 500 nm range the two thin samples exhibit proportionately higher nonradiative energy conversion than the thick samples, when compared to the respective η_{NR} magnitudes for $\lambda \lesssim 500$ nm. These thermal energy releases are most likely to be due to efficient surface absorption layers, which convert the optical energy into heat thus significantly decreasing the luminescence efficiency. Surface absorption layers, as a much more significant fraction of the total thickness (and optical path length) of the thin samples, are also seen to be efficient "nonradiative surface layers" (NRSL), in the context of the $\eta_{NR}(\lambda)$ spectra. They cause severe optical losses by converting a far greater fraction of the available optical energy to heat. On the other hand, bulk absorption and energy conversion processes are expected to dominate in the thick crystals, with NRSL's contributing proportionately much less to thermal energy genera-

tion than in the thin samples. Therefore, the optical quality of the Ti:sapphire material can be immediately assessed from the magnitude of the ratio of $\eta_{NR}(\lambda_2)/\eta_{NR}(\lambda_{min})$ values, where λ_{min} is the wavelength at which the minimum η_{NR} value occurs, and $\lambda_2 > \lambda_{min}$ is some (fixed) wavelength in the spectral region below the fundamental electronic absorption peak, where surface absorption and NRSL effects are expected to be most pronounced. In earlier work Rosencwaig and Hildum[36] determined photoacoustically the η_{NR} of lightly doped Nd^{3+} laser materials, using both microphonic and piezoelectric detection. They used the ratiometric approach,[37] which requires the PAS signal to be measured at two absorbing wavelengths, λ_i and λ_j. The nonradiative (and thus its complement, the radiative) quantum efficiency can then be extracted from the ratio of the two PAS signals, provided that (i) the latter are measured with very high accuracy, (ii) the quantity $(\lambda_j - \lambda_i)$ is as large as possible, and (iii) surface layer absorptions are absent, while incident optical powers and absorption coefficients at λ_i and λ_j are known from independent experiments. Those workers discovered non-negligible surface absorption in their Nd:glass (Ed-2 silicate) samples. In fact, at the Ar^+-ion laser wavelengths of 476.5 and 514.5 nm, the microphonic PAS signals were found to be *predominantly due to surface absorption,* with significant surface contributions even in ultraclean samples. In an experimental configuration resembling our PPE (transmission) detection geometry, the piezoelectric PAS signals contained a much lower contribution from the surface absorptions, due to the backsurface detection character of that contacting technique. In order to obtain that information, however, specific wavelengths had to be chosen at which the sample exhibited the same optical absorption profiles, so as to minimize the effects of different photothermal spatial profiles in the PAS signal amplitude and phase. Similar correction procedures were followed by Quimby and Yen[13] and by Shand.[14] The assumption of strong surface absorptions in our thin disk samples may also be able to account for the anomalous secondary peaks in the near-peak absorption region of Fig. 6. It is tentatively hypothesized that these peaks are due to optical interference phenomena within a surface-damage layer of finite thickness, most likely the results of mechanical polishing of the crystals. In light of the spectral profiles of Fig. 9, it is now apparent that the earlier assumptions of spectrally constant $\eta_{NR}(\lambda)$, which justified the use of the ratiometric approach and the equations therein[36,37] must be reexamined and corrections made for all but, perhaps, the closest probe wavelengths λ_i and λ_j. The recent work by Li *et al.*[33,34] must also be reexamined in terms of the effects of surface absorptions leading to NRSL's in their cut $Ti^{3+}:Al_2O_3$ crystals. It is well known that dc temperature fields do not have the ability to discriminate between surface and bulk transport, since they do not use controlled spatial heat deposition, unlike thermal waves. Therefore, one usually obtains primarily bulk optical-to-thermal energy conversion coefficients with dc heating, since the surface inhomogeneous layer does not enter into a weighed spatial average. Nevertheless, the absolute value of this coefficient may be in error when calculated from dc measurements[33] because the surface heat source (i.e., a NRSL) determines the absolute magnitude of the temperature field in the bulk of the crystal due to efficient heat conduction. As an example, the presence of a truly effective NRSL would require a small increase in optical pump power at the transparent site to raise the *surface temperature* (measured by a thermocouple or a thermistor) to the level of that measured under absorption by the blackened portion of the surface. As a result, a misleadingly high η_{NR} would be calculated, which would be subsequently assumed to represent the actual value throughout the sample bulk, although the latter may be substantially lower. The spectral behavior of the thus measured η_{NR} would be dominated by the bulk and can be very useful qualitatively. Of course, frequency-scanned thermal-wave measurements such as those presented in this work can probe both bulk and surface η_{NR} contributions[36] and may, therefore, be used to separate them out, when coupled with spectroscopic measurements. This work is under development with our $Ti^{3+}:Al_2O_3$ samples and will be reported in a future publication.

The present noncontact PPES technique offers very satisfactory spectral fidelity (reproducibility) of $\eta_{NR}(\lambda)$ absolute values, although the quadrature signals, S_Q, are 2 orders of magnitude lower than the IP, purely optical heating, signals. Figure 10 shows the variances observed in separate experiments using the lowest η_{NR}-producing samples, the thick $Ti^{3+}:Al_2O_3$ crystals. This high degree of experimental accuracy is expected to allow meaningful measurements of $\eta_{NR}(\lambda)$ in the challenging case of laser materials, in general, as well as catalyze developments in the theoretical understanding of this quantity. Contact PPES cannot offer the degree of reproducibility shown in

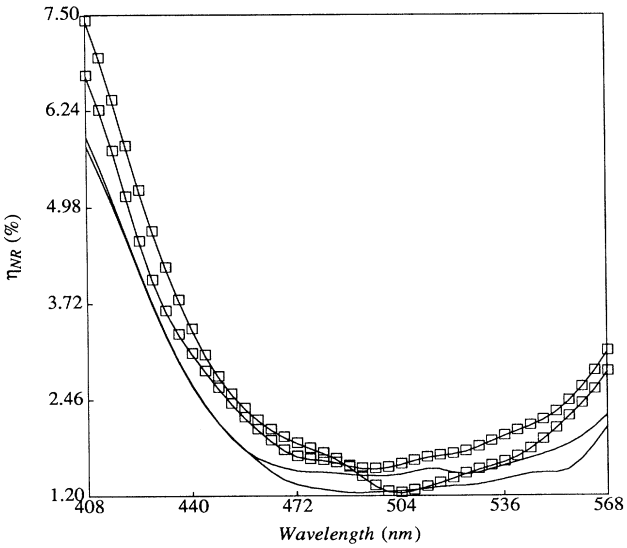

FIG. 10. Experimental spectral variances of $\eta_{NR}(\lambda)$ values calculated from separate experimental runs. (□-□-□), thick Ti:sapphire sample (FOM=800); (——), thick Ti:sapphire sample (FOM=40).

Fig. 10, due to the large variances in thermal contact resistance from one experiment to the next, which totally dominate very weak thermal-wave S_Q signals[36] such as those on which the spectra of Fig. 10 are based.

Preliminary attempts at identifying the origins of the $\eta_{NR}(\lambda)$ responses of the absorption band indicate a high degree of complexity below the metastable level absorption threshold. Following optical absorption and $^2T \rightarrow {}^2E$ electronic excitation, there should be fast nonradiative transitions ("fast heat") to the long-lived metastable level with $\sim 3.3-3.8$-μs lifetime at room temperature.[19,29] Between laser-active levels only heat governed by the nonradiative transition probability-quantum efficiency of the Ti^{3+} ion in the Al_2O_3 host should be released ("slow heat"). On the time scale of our modulated experiments ($T=f^{-1}=0.1$ s) both thermal decays appear instantaneously. Thus, η_{NR} is expected to be in a four-level laser system:

$$\eta_{NR}(\hbar\omega_{3,0}) = \eta_{3,2}(E_{3,2}/E_{3,0}) + \left[\frac{W_{NR}}{W_R + W_{NR}}\right](E_{2,1}/E_{3,0}) + \eta_{1,0}(E_{1,0}/E_{3,0}) + \eta_s(E_3) , \quad (22)$$

where E_0 indicates the ground state and $E_{3,0}$ is the absorbed photon energy: $\hbar\omega_{3,0}=E_3-E_0$, W_R (W_{NR}) is the radiative (nonradiative) emission probability of the upper laser level, and $\eta_{j+1,j}$ is the nonradiative energy-conversion efficiency between levels $(j+1)$ and (j). The term $\eta_s(E_3)$ due to the presence of NRSL's has been added in Eq. (22) with no *a priori* knowledge of its effect, magnitude, or spectral behavior. The structure of Eq. (22) shows that for photon energies above the metastable level $\eta_{NR}(E_3)$ should decrease with decreasing energy E_3 and the first term on the right-hand side becomes zero when $E_3=E_2$. This trend is in agreement with Figs. 9(a) and 9(b) for $\hbar\omega \gtrsim 2.6$ eV ($\sim$490 nm). At $\hbar\omega \sim E_{2,0}$ the $\eta_{NR}(\hbar\omega)$ spectrum is expected to be most sensitive to the ratio $W_{NR}/(W_R+W_{NR}) \equiv \eta_{NR}^{(Q)}$, i.e., to the nonradiative quantum efficiency of the laser medium, a small number in high-quality optical materials [e.g., ruby, 5–10 %;[13,17] alexandrite, 0–5 % (Ref. 14). Below $E_{2,0}$ the value of η_{NR} may rise again, since it only depends on the last two terms on the rhs of Eq. (22). These trends are also in agreement with Fig. 9. The effects of $\eta_s(\hbar\omega)$ seem to be dominant at the low-energy end, as witnessed by the large variances in spectral profiles across our set of samples in this region. Regarding the spectral minima in the $\eta_{NR}(\hbar\omega)$ curves as indicative of $\eta_{NR}^{(Q)}$, an upper limit in that quantity may be calculated without further knowledge of $\eta_s(\hbar\omega)$:

$$\eta_{NR}[(\hbar\omega)_{min}] \geq \eta_{NR}^{(Q)}\left[\frac{E_{2,1}}{E_{2,0}}\right] . \quad (23)$$

For Ti^{3+}:Al_2O_3 we may take the peak of the fluorescence spectrum at 760 nm (Ref. 19) as $\bar{E}_{2,1}$ and $E_{2,0} \sim (\hbar\omega)_{min}$. This yields, from Fig. 9,

$$\begin{aligned} &\eta_{NR}^{(Q)}(Ti^{3+}:Al_2O_3)_{thin;FOM=40} \lesssim 13.80005 , \\ &\eta_{NR}^{(Q)}(Ti^{3+}:Al_2O_3)_{thin;FOM=800} \lesssim 12.70005 , \\ &\eta_{NR}^{(Q)}(Ti^{3+}:Al_2O_3)_{thick;FOM=40} \lesssim 1.90005 , \\ &\eta_{NR}^{(Q)}(Ti^{3+}:Al_2O_3)_{thick;FOM=800} \lesssim 2.40005 . \end{aligned} \quad (24)$$

Detailed theoretical models of the Ti^{3+}:Al_2O_3 system are currently under investigation,[20,21] extended to incorporate $\eta_{NR}(\hbar\omega)$ and $\eta_{NR}^{(Q)}$ information for better quantification of the latter quantity and for our understanding of the role of NRSL's.

VI. CONCLUSIONS

A sensitive noncontact photopyroelectric (PPES) technique was developed theoretically and experimentally. This technique was applied to the Ti:sapphire laser material system and a matrix of industrial crystals was studied. The efficient suppression of the direct optical heating mode of this PPES technique has allowed purely thermal-wave signal (quadrature) monitoring generated by *minute* optical-to-thermal (nonradiative) energy conversions in high-quality Ti:sapphire samples. Bulk- and surface-originating high-resolution spectra of these materials' nonradiative energy-conversion efficiencies were obtained with a single experimental configuration and an excellent degree of fidelity (reproducibility), despite the extremely low signal levels. These spectra exhibited a strong variation across the visible range, thus bringing into question earlier assumptions on the spectral constancy of nonradiative (and, therefore, radiative) energy efficiencies in photothermal measurements of these quantities in optical materials. Contributions to the absorption and nonradiative spectra from the polished crystal surfaces were found to be substantial and the concept of "nonradiative surface layer" was introduced to define the surface localization of the optical-to-thermal energy conversion effects. The nonradiative spectra are in essential agreement with simple energy decay considerations in four-level laser media. The $\eta_{NR}(\lambda)$ spectral profiles, besides their intrinsic fundamental interest, can be used as efficient criteria of Ti:sapphire optical quality for industrial crystal growth and process control, including post-growth annealing and laser rod fabrication.

ACKNOWLEDGMENTS

We gratefully acknowledge a Strategic Grant from the Natural Sciences and Engineering Research Council of Canada (NSERC), which made this work possible. The assistance of V. Yang and P. Wong with some of the measurements is also acknowledged.

APPENDIX: POLAR-COORDINATE COMPONENTS OF EQ. (18a)

(1) Amplitude components:

$$|Z_1|=[1+(\beta^2/2a_s^2)^2]^{1/2}\ , \tag{A1}$$

$$|Z_2|=\{[1-\gamma_{gs}^2 e^{-2a_gL}\cos(2a_gL)]^2+\gamma_{gs}^4 e^{-4a_gL}\sin^2(2a_gL)\}^{1/2}\ , \tag{A2}$$

$$|Z_3|=\left[\left[1-\gamma_{gs}\gamma_{gp}\frac{|Q_1|}{|Z_2|}e^{-2a_gL}\cos(\phi_1-\phi_2-2a_gL)\right]^2+\gamma_{gs}^2\gamma_{gp}^2\left[\frac{|Q_1|}{|Z_2|}\right]^2 e^{-4a_gL}\sin^2(\phi_1-\phi_2-2a_gL)\right]^{1/2}\ , \tag{A3a}$$

where

$$|Q_1|=\{[1-e^{-2a_sl}\cos(2a_sl)]^2+e^{-4a_sl}\sin^2(2a_sl)\}^{1/2}\ , \tag{A3b}$$

$$\phi_1=\tan^{-1}\left[\frac{e^{-2a_sl}\sin(2a_sl)}{1-e^{-2a_sl}\cos(2a_sl)}\right]\ , \tag{A3c}$$

and

$$\phi_2=\tan^{-1}\left[\frac{\gamma_{gs}^2 e^{-2a_sl}\sin(2a_sl)}{1-\gamma_{gs}^2 e^{-2a_sl}\cos(2a_sl)}\right]\ , \tag{A3d}$$

$$|Z_4|=\left\{\left[\frac{1}{\sqrt{2}}|r_s|(N_1-N_2e^{-2\beta l})+b_{gs}(N_1+N_2e^{-2\beta l})\right]^2+\frac{1}{2}|r_s|^2(N_1-N_2e^{-2\beta l})^2\right\}^{1/2}\ , \tag{A4}$$

$$|Z_5|=\left\{\left[\frac{1}{\sqrt{2}}|r_s|(N_1-N_2)+N_1+N_2\right]^2+\frac{1}{2}|r_s|^2(N_1-N_2)^2\right\}^{1/2}\ , \tag{A5}$$

$$|Z_6|=\left\{\left[N_1+N_2-\frac{1}{\sqrt{2}}|r_s|(N_1-N_2)\right]^2+\frac{1}{2}|r_s|^2(N_1-N_2)^2\right\}^{1/2}\ . \tag{A6}$$

(2) Phase components:

$$\psi_1=\phi_2-\phi_3+\phi_4+\phi_5+a_gL+a_sl+\frac{\pi}{4}\ , \tag{A7a}$$

where

$$\phi_3=\tan^{-1}\left[\frac{-|r_s|(N_1-N_2e^{-2\beta l})}{|r_s|(N_1-N_2e^{-2\beta l})+\sqrt{2}b_{gs}(N_1+N_2e^{-2\beta l})}\right]\ , \tag{A7b}$$

$$\phi_4=\tan^{-1}\left[\frac{-\gamma_{gs}\gamma_{gp}(|Q_1|/|Z_2|)e^{-2a_gL}\sin(\phi_1-\phi_2-2a_gL)}{1-\gamma_{gs}\gamma_{gp}(|Q_1|/|Z_2|)e^{-2a_gL}\cos(\phi_1-\phi_2-2a_gL)}\right]\ , \tag{A7c}$$

$$\phi_5=\pi+\tan^{-1}\left[\frac{1}{\sqrt{2}}|r_s|\right]\ , \tag{A7d}$$

where

$$\psi_2=\phi_2+\phi_4+\phi_5-\phi_6+a_gL+\frac{\pi}{4}\ , \tag{A8a}$$

where

$$\phi_6=\tan^{-1}\left[\frac{-|r_s|(N_1-N_2)}{|r_s|(N_1-N_2)+\sqrt{2}(N_1+N_2)}\right]\ , \tag{A8b}$$

$$\psi_3=\phi_2+\phi_4+\phi_5-\phi_7+a_gL+2a_sl+\frac{\pi}{4}\ , \tag{A9a}$$

$$\phi_7=\tan^{-1}\left[\frac{|r_s|(N_1-N_2)}{\sqrt{2}(N_1+N_2)-|r_s|(N_1-N_2)}\right]\ . \tag{A9b}$$

[1]L. D. Merkle and R. C. Powell, Chem. Phys. Lett. **46**, 303 (1977).
[2]F. Auzel, D. Meichenin, and J. C. Michel, J. Lumin. **18/19**, 97 (1979).
[3]R. G. Peterson and R. C. Powell, Chem. Phys. Lett. **53**, 366 (1978).
[4]R. S. Quimby and W. M. Yen, Opt. Lett. **3**, 181 (1978).
[5]R. C. Powell, D. P. Neikirk, J. M. Flaherty, and J. G. Gualtieri, J. Phys. Chem. Solids **41**, 345 (1980).
[6]A. Mandelis, Chem. Phys. Lett. **91**, 501 (1982).
[7]M. G. Rockley and K. M. Waugh, Chem. Phys. Lett. **54**, 597 (1978).
[8]J. L. Laporte, B. Bonno, and Y. Rousset, J. Photochem. Photobiol. A **45**, 215 (1988).
[9]J. Etxebarria and J. Fernández, J. Phys. C **16**, 3803 (1983).
[10]M. Grinberg, A. Mandelis, K. Fjeldsted, and A. Othonos, Phys. Rev. B **48**, 5922 (1993).
[11]M. Grinberg, A. Mandelis, and K. Fjeldsted, Phys. Rev. B **48**, 5935 (1993).
[12]A. Mandelis and B. S. H. Royce, J. Opt. Soc. Am. **70**, 474 (1980).
[13]R. S. Quimby and W. M. Yen, J. Appl. Phys. **51**, 1780 (1980).
[14]M. L. Shand, J. Appl. Phys. **54**, 2602 (1983).
[15]G. A. R. Lima, M. L. Baesso, Z. P. Arguello, E. C. da Silva, H. Vargas, and L. C. M. Miranda, Phys. Rev. B **36**, 9812 (1987).
[16]A. Rosencwaig and A. Gersho, J. Appl. Phys. **47**, 64 (1976).
[17]A. Mandelis, M. Munidasa, and A. Othonos, IEEE J. Quant. Electron. (to be published).
[18]A. Mandelis and M. Munidasa (unpublished).
[19]P. Albers, E. Stark, and G. Huber, J. Opt. Soc. Am. B **3**, 134 (1986).
[20]A. Mandelis and M. M. Zver, J. Appl. Phys. **57**, 4421 (1985).
[21]A. Mandelis, R. E. Wagner, K. Ghandi, R. Baltman, and P. Dao, Phys. Rev. B **39**, 5254 (1989).
[22]J. Fan and J. Kakalios, Philos. Mag. Lett. **64**, 235 (1991).
[23]C. Christofides, A. Mandelis, and K. Ghandi, Rev. Sci. Instrum. **61**, 2360 (1990).
[24]H. Coufal, Appl. Phys. Lett. **45**, 516 (1984).
[25]Y. Dupin, Z. Angru, and W. Zhaoyong, J. Phys. D **21**, 641 (1988).
[26]C. Christofides, A. Mandelis, A. Engel, M. Bisson, and G. Harling, Can. J. Phys. **69**, 317 (1991).
[27]E. H. Putley, in *Semiconductors and Semimetals,* edited by R. K. Willardson and A. C. Beer (Academic, New York, 1970), Vol. 5, Chap. 6, p. 259.
[28]P. A. Schultz and S. R. Henion, IEEE J. Quant. Electron. **QE-27**, 1039 (1991).
[29]P. Lacovara, L. Esterowitz, and M. Kokta, IEEE J. Quant. Electron. **QE-21**, 1614 (1985).
[30]Kynar® Piezo Film *Technical Manual* (Pennwalt, King-of-Prussia, PA, 1983); for other ferroelectrics, *Proceedings of the 6th International Symposium on Electrets,* Oxford, 1988, edited by D. K. Das Gupta and A. Patullo (IEEE Service Center, Piscataway, N.J., 1988).
[31]L. J. Andrews, A. Lempecki, and B. C. McCollum, J. Chem. Phys. **74**, 5526 (1981).
[32]C. E. Byvik, A. M. Buoncristiani, S. J. McMurray, and M. Kokta, in *Tunable Solid-State Lasers II,* edited by A. B. Budgor, L. Esterowitz, and L. G. DeShazer (Springer-Verlag, New York, 1986), p. 242.
[33]Y. Li, I. Duncan, and T. Morrow, J. Lumin. **50**, 69 (1991).
[34]Y. Li, I. Duncan, and T. Morrow, J. Lumin. **52**, 275 (1992).
[35]P. F. Moulton, J. Opt. Soc. Am. B **3**, 125 (1986).
[36]A. Rosencwaig and E. A. Hildum, Phys. Rev. B **23**, 3301 (1981).
[37]M. G. Rockley, Chem. Phys. Lett. **50**, 427 (1977).
[38]A. daSilva, M.Sc.E. Thesis, University of Toronto, 1993.